

## Mode interactions in an enclosed swirling flow: a double Hopf bifurcation between azimuthal wavenumbers 0 and 2

By F. MARQUES<sup>1</sup>, J. M. LOPEZ<sup>2</sup> AND J. SHEN<sup>3</sup>

<sup>1</sup>Departament de Física Aplicada, Universitat Politècnica de Catalunya, Jordi Girona Salgado s/n, Mòdul B4 Campus Nord, 08034 Barcelona, Spain

<sup>2</sup>Department of Mathematics, Arizona State University, Tempe, AZ 85287, USA

<sup>3</sup>Department of Mathematics, University of Central Florida, Orlando, FL 32816-1632, USA

(Received 27 November 2000 and in revised form 27 June 2001)

A double Hopf bifurcation has been found of the flow in a cylinder driven by the rotation of an endwall. A detailed analysis of the multiple solutions in a large region of parameter space, computed with an efficient and accurate three-dimensional Navier–Stokes solver, is presented. At the double Hopf point, an axisymmetric limit cycle and a rotating wave bifurcate simultaneously. The corresponding mode interaction generates an unstable two-torus modulated rotating wave solution and gives a wedge-shaped region in parameter space where the two periodic solutions are both stable. By exploring in detail the three-dimensional structure of the flow, we have identified the two mechanisms that compete in the neighbourhood of the double Hopf point. Both are associated with the jet that is formed when the Ekman layer on the rotating endwall is turned by the stationary sidewall.

---

### 1. Introduction

The flow in an enclosed right-circular cylinder of height  $H$  and radius  $R$ , filled with an incompressible fluid of kinematic viscosity  $\nu$ , and driven by the constant rotation,  $\Omega \text{ rad s}^{-1}$ , of one of its endwalls has been widely studied (e.g. Escudier 1984; Lugt & Abboud 1987; Neitzel 1988; Daube & Sørensen 1989; Lopez 1990; Lopez & Perry 1992; Sørensen & Christensen 1995; Gelfgat, Bar-Yoseph & Solan 1996; Spohn, Mory & Hopfinger 1998; Stevens, Lopez & Cantwell 1999; Blackburn & Lopez 2000; Sotiropoulos & Ventikos 2001; Gelfgat, Bar-Yoseph & Solan 2001). The main motivation for these studies has been that over a range of the governing parameters,  $Re = \Omega R^2/\nu$  and  $A = H/R$ , there exist flow states with recirculation zones located on the central vortex, commonly referred to as vortex breakdown bubbles. In spite of the numerous numerical and experimental studies, there continues to be considerable controversy concerning fundamental aspects of this flow, particularly with the question of if and how the basic state (steady and axisymmetric) breaks symmetry.

The governing equations, Navier–Stokes and conservation of mass, together with the boundary conditions, no-slip on all solid walls and regularity on the cylinder axis, are invariant with respect to rotations about the axis. The system possesses the symmetry group  $SO(2)$ . The basic state for this system is a steady axisymmetric

swirling flow with non-trivial structure in  $r$  and  $z$ , the radial and axial coordinates. The only observed, either experimentally or computationally, codimension-one local bifurcations of the basic state are Hopf bifurcations that either preserve or break the  $SO(2)$  symmetry, depending on where in parameter space the system is investigated. When  $SO(2)$  is preserved a time-dependent axisymmetric state results (e.g. Escudier 1984; Lopez & Perry 1992; Stevens *et al.* 1999). The linear stability analysis of Gelfgat *et al.* (2001) predicts that there are regions of parameter state where the Hopf bifurcation breaks  $SO(2)$ , leading to a rotating wave (Knobloch 1994, 1996). As a consequence, it may be expected that there are codimension-two points where the two types of Hopf coincide, i.e. double Hopf points. Since there are only two parameters involved, the system can be expected to generically only display either codimension-one or codimension-two bifurcations. The general theory of double Hopf bifurcations has been elaborated (e.g. Guckenheimer & Holmes 1986; Kuznetsov 1998), and there are many possible scenarios depending on the particulars of the system at hand. The equivariant double Hopf bifurcation with either  $SO(2)$  (invariance to azimuthal rotations) or  $O(2)$  (invariance to azimuthal rotations and to reflections through a meridional plane) has been studied (e.g. Knobloch & Proctor 1988; Renardy *et al.* 1996), but these have been mostly in resonant situations. We show in the Appendix that when the system possesses  $SO(2)$  symmetry then resonances are inhibited (vis-a-vis the generic case), and in particular, when one of the Hopf bifurcations preserves  $SO(2)$  then there can be no resonances; this is the situation predicted by Gelfgat *et al.* (2001) for  $A < 1.7$  and is studied here via full nonlinear computations of the three-dimensional Navier–Stokes equations.

The extensive details that full nonlinear three-dimensional computations provide have been used here to extract the physical mechanisms leading to the two distinct types of Hopf bifurcations. Also, at the double Hopf point, there may be states that bifurcate that are not predicted directly from a linear stability analysis (e.g. two-tori solutions), and originating at the double Hopf point is an extensive region in parameter space where multiple stable solutions coexist.

## 2. Background on double Hopf bifurcation

The double Hopf bifurcation, which is readily located via linear stability analysis as the codimension-two point at which two pairs of complex conjugate eigenvalues have their real part simultaneously change sign, has associated very rich nonlinear dynamics in its neighbourhood. Depending on the particulars of the system under consideration, there are around thirty different dynamical scenarios, divided into *simple* and *difficult* cases. For our flow, we shall show that the simplest of the simple cases is manifested.

For codimension-one and some codimension-two bifurcations, dynamical systems theory provides a *normal form*, a low-dimensional, low-order polynomial system that captures the dynamics of the full nonlinear system. Arbitrary perturbations of the normal form result in a topologically equivalent system preserving all the dynamics of the normal form. When the codimension of the system is two or greater, persistence of the normal form is not always guaranteed. One may still perform a normal form analysis on the original system, truncating at some finite (low) order and extract some of the characteristic dynamics of the original system; however this formal application of the theory results in a *formal normal form* with, in general, some dynamical features that do not persist upon perturbation. The double Hopf bifurcation is a typical example where the dynamics of the formal normal form do not always persist.

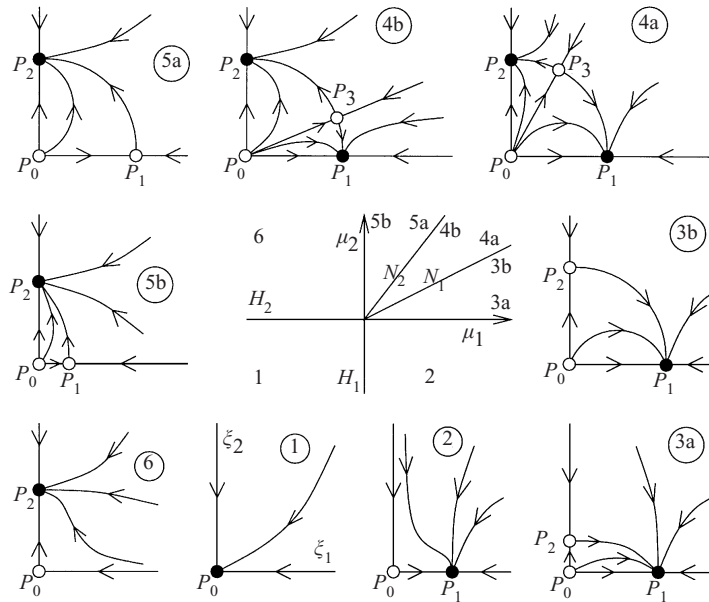


FIGURE 1. Bifurcation diagram of the double Hopf bifurcation, in normal form variables, corresponding to the present flow. Solid (●) and hollow (○) dots correspond to stable and unstable solutions respectively,  $\mu_{1,2}$  are the two bifurcation parameters,  $H_{1,2}$  are the two Hopf curves, and  $N_{1,2}$  are the two Naimark–Sacker curves.

The infinite-dimensional phase space of our problem, in certain regions of parameter space, admits a four-dimensional centre manifold parameterized by a pair of amplitudes  $r_{1,2}$  and angles  $\phi_{1,2}$ . The normal form is given by (Kuznetsov 1998)

$$\left. \begin{aligned} \dot{r}_1 &= r_1(\mu_1 + p_{11}r_1^2 + p_{12}r_2^2 + s_1r_2^4), \\ \dot{r}_2 &= r_2(\mu_2 + p_{21}r_1^2 + p_{22}r_2^2 + s_2r_1^4), \\ \dot{\phi}_1 &= \omega_1, \\ \dot{\phi}_2 &= \omega_2, \end{aligned} \right\} \quad (2.1)$$

where  $\mu_{1,2}$  are the normalized bifurcation parameters and the two pairs of complex conjugate eigenvalues are  $\pm i\omega_{1,2}$  at the bifurcation point  $\mu_{1,2} = 0$ . The  $\omega_{1,2}$ ,  $p_{ij}$ , and  $s_i$  depend on the parameters  $\mu_{1,2}$  and satisfy certain non-degeneracy conditions in the neighbourhood of the bifurcation:

- (a)  $k\omega_1 \neq l\omega_2$ ,  $k, l > 0$ ,  $k + l \leq 5$ ,
- (b)  $p_{ij} \neq 0$ .

The normal form (2.1) admits a multitude of distinct dynamical behaviour, depending on the values of  $p_{ij}$  and  $s_i$ . These are divided into so-called *simple* ( $p_{11}p_{22} > 0$ ) and *difficult* ( $p_{11}p_{22} < 0$ ) cases. In the simple cases, the topology of the bifurcation diagram is independent of the  $s_i$  terms. Even in the simple case, ten different bifurcation diagrams exist. A comprehensive description of all the simple and difficult scenarios is in Kuznetsov (1998).

For the Navier–Stokes flow example studied here, we shall demonstrate that it possesses a double Hopf bifurcation of the simple type with the corresponding diagram given in figure 1. For this simple case, a convenient rescaling of (2.1) leads

to the normal form

$$\dot{\xi}_1 = \xi_1(\mu_1 - \xi_1 - \eta\xi_2), \quad \dot{\xi}_2 = \xi_2(\mu_2 - \delta\xi_1 - \xi_2), \quad (2.2)$$

plus the trivial equations for the corresponding phases  $\phi_i$ . This normal form does not contain the quintic terms that are present in (2.1); they only affect the normal form in the difficult case Kuznetsov 1998. The figure corresponds to  $\eta > 0$ ,  $\delta > 0$  and  $\eta\delta > 1$ . The values of  $\eta$  and  $\delta$  and the relationships between  $(\mu_1, \mu_2)$  and  $(Re, A)$  corresponding to the double Hopf bifurcation in our flow will be determined in §4. The normal forms (2.1) and (2.2) are generic in the sense that no symmetry considerations were imposed in their derivation. Although our system has  $SO(2)$  symmetry, we show in the Appendix that this symmetry, under certain non-resonance conditions, does not alter the normal form, and in fact that the  $SO(2)$  symmetry prohibits resonances in the case of one Hopf bifurcation preserving the symmetry and the other breaking it, which is the particular double Hopf bifurcation for our system.

The phase portraits in figure 1 are projections onto  $(\xi_1, \xi_2)$ , and rotation about each axis recovers angle information. The origin is a fixed point ( $P_0$ ), corresponding to the steady axisymmetric base state (Lopez 1990; Lopez, Marques & Sanchez 2001a). The fixed point on the  $\xi_1$ -axis ( $P_1$ ) corresponds to an  $SO(2)$  equivariant limit-cycle solution (Lopez & Perry 1992; Stevens *et al.* 1999; Lopez *et al.* 2001a). The fixed point on the  $\xi_2$ -axis ( $P_2$ ) corresponds to another limit cycle which is not  $SO(2)$  equivariant; it is a pure rotating wave (Gelfgat *et al.* 2001). The fixed point off the axis ( $P_3$ ) is an unstable, saddle two-torus which is  $SO(2)$  equivariant, although solutions on it are not; they are (unstable) modulated rotating waves. The parametric portrait in the centre of the figure consists of six distinct regions separated by Hopf bifurcation curves,  $H_1$  and  $H_2$ , and Naimark–Sacker bifurcation (Hopf bifurcation for limit cycles) curves,  $N_1$  and  $N_2$ . In region 1, the only fixed point,  $P_0$ , is the steady axisymmetric basic state. As  $\mu_1$  changes sign to positive,  $P_0$  loses stability via a supercritical Hopf bifurcation and a stable axisymmetric limit cycle,  $P_1$ , emerges (region 2). When  $\mu_2$  becomes positive,  $P_0$  undergoes a second Hopf bifurcation and an unstable rotating wave,  $P_2$ , emerges (region 3). On further parameter variation across the line  $N_1$ , the unstable rotating wave undergoes a Naimark–Sacker bifurcation, becomes stable and an unstable modulated rotating wave,  $P_3$ , emerges (region 4). In region 4, there coexist two stable states,  $P_1$  and  $P_2$ , and two unstable states,  $P_0$  and  $P_3$ . Crossing  $N_2$ ,  $P_3$  collides with  $P_1$  in another Naimark–Sacker bifurcation in which the modulated rotating wave vanishes and the axisymmetric limit cycle,  $P_1$ , becomes unstable (region 5). On entering region 6, the unstable  $P_1$  collides with the unstable basic state,  $P_0$ , in a supercritical Hopf bifurcation and vanishes;  $P_0$  remains unstable. Finally, entering region 1, the stable rotating wave,  $P_2$ , collides with  $P_0$ , in a supercritical Hopf bifurcation with  $P_2$  vanishing and  $P_0$  becoming stable.

The above scenario is now demonstrated for the swirling cylinder flow via direct computations of the fully nonlinear three-dimensional Navier–Stokes equations, showing that the above low-dimensional dynamical systems theory describes the dynamics of the physical system in a neighbourhood of the double Hopf point. Adding higher-order terms to the double-Hopf normal form generically does not result in a topologically equivalent system. However, the fixed points and limit cycles are robust, and the Hopf and Naimark–Sacker curves persist (Kuznetsov 1998). The two-torus is also robust, but the orbit structure on it (e.g. quasi-periodicity, phase locking) may be altered. Other dynamics, such as homoclinic and heteroclinic bifurcations are also usually altered by higher-order terms, but these are not present in the simple scenario that corresponds to our swirling cylinder flow.

### 3. Navier–Stokes equations and the numerical scheme

We consider an incompressible flow confined in a cylinder, i.e. the domain in cylindrical coordinates  $(r, \theta, z)$  is

$$\mathcal{D} = \{0 \leq r < R, \quad 0 \leq \theta < 2\pi, \quad 0 < z < H\}.$$

The equations governing the flow are the Navier–Stokes equations together with initial and boundary conditions. We denote the velocity vector and pressure respectively by  $\mathbf{u} = (u, v, w)^T$  and  $p$ . Then, the Navier–Stokes equations in velocity–pressure formulation written in cylindrical coordinates, and non-dimensionalized using  $R$  as the length scale and  $1/\Omega$  as the time scale, are

$$\left. \begin{aligned} \partial_t u + \text{adv}_r &= -\partial_r p + \frac{1}{Re} \left( \Delta u - \frac{1}{r^2} u - \frac{2}{r^2} \partial_\theta v \right), \\ \partial_t v + \text{adv}_\theta &= -\partial_\theta p + \frac{1}{Re} \left( \Delta v - \frac{1}{r^2} v + \frac{2}{r^2} \partial_\theta u \right), \\ \partial_t w + \text{adv}_z &= -\partial_z p + \frac{1}{Re} \Delta w, \end{aligned} \right\} \quad (3.1)$$

$$\frac{1}{r} \partial_r (ru) + \frac{1}{r} \partial_\theta v + \partial_z w = 0, \quad (3.2)$$

where

$$\Delta = \partial_r^2 + \frac{1}{r} \partial_r + \frac{1}{r^2} \partial_\theta^2 + \partial_z^2 \quad (3.3)$$

is the Laplace operator in cylindrical coordinates and

$$\left. \begin{aligned} \text{adv}_r &= u \partial_r u + \frac{v}{r} \partial_\theta u + w \partial_z u - \frac{v^2}{r}, \\ \text{adv}_\theta &= u \partial_r v + \frac{v}{r} \partial_\theta v + w \partial_z v - \frac{uv}{r}, \\ \text{adv}_z &= u \partial_r w + \frac{v}{r} \partial_\theta w + w \partial_z w. \end{aligned} \right\} \quad (3.4)$$

The equations are to be completed with admissible initial and boundary conditions.

Note that in addition to the nonlinear coupling, the velocity components  $(u, v)$  are also coupled by the linear operators in this case. Following Orszag & Patera (1983), we introduce a new set of complex functions

$$u_+ = u + iv, \quad u_- = u - iv. \quad (3.5)$$

Note that

$$u = \frac{1}{2}(u_+ + u_-), \quad v = \frac{1}{2i}(u_+ - u_-). \quad (3.6)$$

The Navier–Stokes equations (3.1)–(3.2) can then be written using  $(u_+, u_-, w, p)$  as

$$\left. \begin{aligned} \partial_t u_+ + \text{adv}_+ &= - \left( \partial_r + \frac{i}{r} \partial_\theta \right) p + \frac{1}{Re} \left( \Delta - \frac{1}{r^2} + \frac{2i}{r^2} \partial_\theta \right) u_+, \\ \partial_t u_- + \text{adv}_- &= - \left( \partial_r - \frac{i}{r} \partial_\theta \right) p + \frac{1}{Re} \left( \Delta - \frac{1}{r^2} - \frac{2i}{r^2} \partial_\theta \right) u_-, \\ \partial_t w + \text{adv}_z &= -\partial_z p + \frac{1}{Re} \Delta w, \end{aligned} \right\} \quad (3.7)$$

---

$Re$	$m = 0$	$m = 2$	$m = 4$	$m = 6$
2615	$2.258 \times 10^{-5}$	$7.928 \times 10^{-9}$	$6.541 \times 10^{-12}$	$1.007 \times 10^{-14}$
2620	$2.259 \times 10^{-5}$	$1.404 \times 10^{-8}$	$2.072 \times 10^{-11}$	$5.687 \times 10^{-14}$
2630	$2.261 \times 10^{-5}$	$2.632 \times 10^{-8}$	$7.205 \times 10^{-11}$	$3.693 \times 10^{-13}$
2650	$2.264 \times 10^{-5}$	$5.000 \times 10^{-8}$	$2.627 \times 10^{-10}$	$2.584 \times 10^{-12}$
2700	$2.272 \times 10^{-5}$	$1.073 \times 10^{-7}$	$1.202 \times 10^{-9}$	$2.566 \times 10^{-11}$
2750	$2.280 \times 10^{-5}$	$1.594 \times 10^{-7}$	$2.703 \times 10^{-9}$	$8.755 \times 10^{-11}$

---

TABLE 1. The  $m = 0$  column shows the time average of the kinetic energy of the zero mode (which is periodic); the other columns show the kinetic energy of the  $m$ -azimuthal mode, for  $A = 1.57$  and  $Re$  as indicated.

$$\left(\partial_r + \frac{1}{r}\right)(u_+ + u_-) - \frac{i}{r}\partial_\theta(u_+ - u_-) + 2\partial_z w = 0, \quad (3.8)$$

where we have denoted

$$\text{adv}_\pm = \text{adv}_r \pm i \text{adv}_\theta. \quad (3.9)$$

The main difficulty in numerically solving the above equations is due to the fact that the velocity vector and the pressure are coupled together through the continuity equation. An efficient way to overcome this difficulty is to use a so-called projection scheme originally proposed by Chorin (1968) and Temam (1969). Here, we use a stiffly stable semi-implicit (i.e. the linear terms are treated implicitly while the nonlinear terms are explicit) second-order projection scheme (see Lopez & Shen 1998; Lopez, Marques & Shen 2001*b*, for more details). For the space variables, we use a Legendre–Fourier approximation. More precisely, the azimuthal direction is discretized using a Fourier expansion with  $k + 1$  modes corresponding to azimuthal wavenumbers  $m = 0, 1, 2, \dots, k/2$ , while the axial and vertical directions are discretized with a Legendre expansion. With the above discretization, one only needs to solve, at each time step, a Poisson-like equation for each of the velocity components and for pressure. These Poisson-like equations are solved using the very efficient spectral-Galerkin method presented in Shen (1994, 1997). In short, as demonstrated in Lopez & Shen (1998) and Lopez *et al.* (2001*b*), the combination of the spectral-Galerkin discretization in space with a semi-implicit second-order projection scheme in time provides a very accurate and efficient algorithm for solving the three-dimensional Navier–Stokes equations in a cylinder.

The spectral convergence of the code in  $r$  and  $z$  has already been extensively described in Lopez & Shen (1998) for  $m = 0$ ; the convergence properties in  $r, z$  are not affected by  $m \neq 0$ . For the convergence in the azimuthal direction, since we are here only interested in solutions near bifurcations, the number of azimuthal modes needed are expected to be small. Table 1 lists the kinetic energy ( $\mathcal{L}_2$ -norm squared of the particular mode,  $E_m$ ) of  $m = 2$  and the first few harmonics over the range of  $Re$  with  $SO(2)$  broken to give an  $m = 2$  rotating wave, as well as that of  $m = 0$  averaged over one period. The first two harmonics have energies at least two and four orders of magnitude smaller than  $m = 2$ , respectively, so inclusion of the next harmonic,  $m = 8$ , does not change the solution. Notice that  $m = 0$  contains the bulk of the energy of the complete flow.

All the results presented here have 64 Legendre modes in  $r$  and  $z$  and 15 Fourier modes in  $\theta$ , and the time-step is  $\delta t = 0.05$ .

## 4. Results

### 4.1. Dynamical systems description of the results

The above algorithm has been applied to a large number of parameter values in the neighbourhood of the double Hopf bifurcation. The solutions have been computed for a time large enough to reach the corresponding asymptotic states; as we are close to the bifurcation point, the transients take a very long time to fade away. We have used a continuation strategy (starting with the closest solution previously obtained) to follow branches of solutions into regions of coexistence. Figure 2(a) shows the computed solutions, indicating also their nature:  $\blacklozenge$  are  $m = 2$  rotating waves,  $\square$  are  $m = 0$  limit cycles, and  $\circ$  are  $m = 0$  steady states. Only the stable solutions are shown (cf. figure 1), as these are the only ones directly computable from an initial value problem, and so the parts of the Hopf curves,  $(\mu_1, \mu_2 > 0)$  and  $(\mu_2, \mu_1 > 0)$ , are not directly determined. Figure 2(b) is a close-up of (a) in the neighbourhood of the double Hopf point. As expected from normal form theory (Kuznetsov 1998), the Hopf and Naimark–Sacker curves are straight lines in this neighbourhood. We can determine an affine transformation from the  $(Re, A)$ -plane to the  $(\mu_1, \mu_2)$ -plane, given by

$$\left. \begin{aligned} \mu_1 &= 3.84(Re - Re_{dH})/Re_{dH} + A - A_{dH}, \\ \mu_2 &= 2.00(Re - Re_{dH})/Re_{dH} - A + A_{dH}, \end{aligned} \right\} \quad (4.1)$$

where  $Re_{dH} = 2627$ ,  $A_{dH} = 1.583$  are the critical values at the double Hopf point; the linear stability analysis of Gelfgat *et al.* (2001) gives  $Re_{dH} \approx 2680$  and  $A_{dH} = 1.63$ , agreeing with our numerics to within 3%. The transformation is determined, except for positive factors in (4.1) that have been fixed to simplify the expressions ( $\pm 1$  in front of  $A$ ). The computation of the normal form parameters,  $\eta$  and  $\delta$ , is now straightforward from the slopes of the  $N_1$  and  $N_2$  curves, giving  $\eta = 2.21$  and  $\delta = 1.20$ , both greater than zero. Although their values depend on the aforementioned factors, their product does not. Their product is an important parameter because it determines which of the possible double-Hopf scenarios corresponds to our system. Since  $\eta\delta = 2.66 > 1$ , our system corresponds to Case I mentioned in Kuznetsov (1998), and displayed in figure 1.

We have verified that the two Hopf bifurcations ( $H_1$  and  $H_2$ ) are supercritical. Figure 3(a) shows the  $\mathcal{L}_2$ -norm squared of the amplitude of the oscillations of the axisymmetric periodic solutions (named  $\bar{E}_0$ ) as they approach the Hopf bifurcation line ( $H_1$ ) from above ( $Re > Re_{crit}$ ), for different  $A$  values. The amplitudes squared go linearly to zero at the bifurcation point, and therefore the amplitudes show the square-root behaviour characteristic of a supercritical Hopf bifurcation. Figure 3(b) displays the same behaviour for the  $\mathcal{L}_2$ -norm squared of the  $m = 2$  mode corresponding to the rotating wave (denoted  $E_2$ ). These diagrams also allow an accurate determination of the critical lines  $H_1$  and  $H_2$ , as the intersections of the displayed straight lines with the horizontal axis.

The  $N_1$  Naimark–Sacker curve is detected by continuing the rotating wave solution across it by increasing  $A$  until it becomes unstable and evolves to the  $m = 0$  limit cycle; figure 4 shows this evolution for  $Re = 2690$  and  $A = 1.590$ . The initial value problem used as the initial condition the stable  $m = 2$  rotating wave solution at  $Re = 2690$ ,  $A = 1.585$ . Figure 4(a) shows that the energy of the axisymmetric component,  $E_0$ , oscillates with an exponentially growing amplitude; when it reaches a certain amplitude, this component draws energy from the  $m = 2$  component (figure 4b shows the exponential decay of  $E_2$ ). The asymptotic state that results is a stable axisymmetric limit cycle. Likewise, the  $N_2$  curve is detected by continuing the  $m = 0$  limit cycle

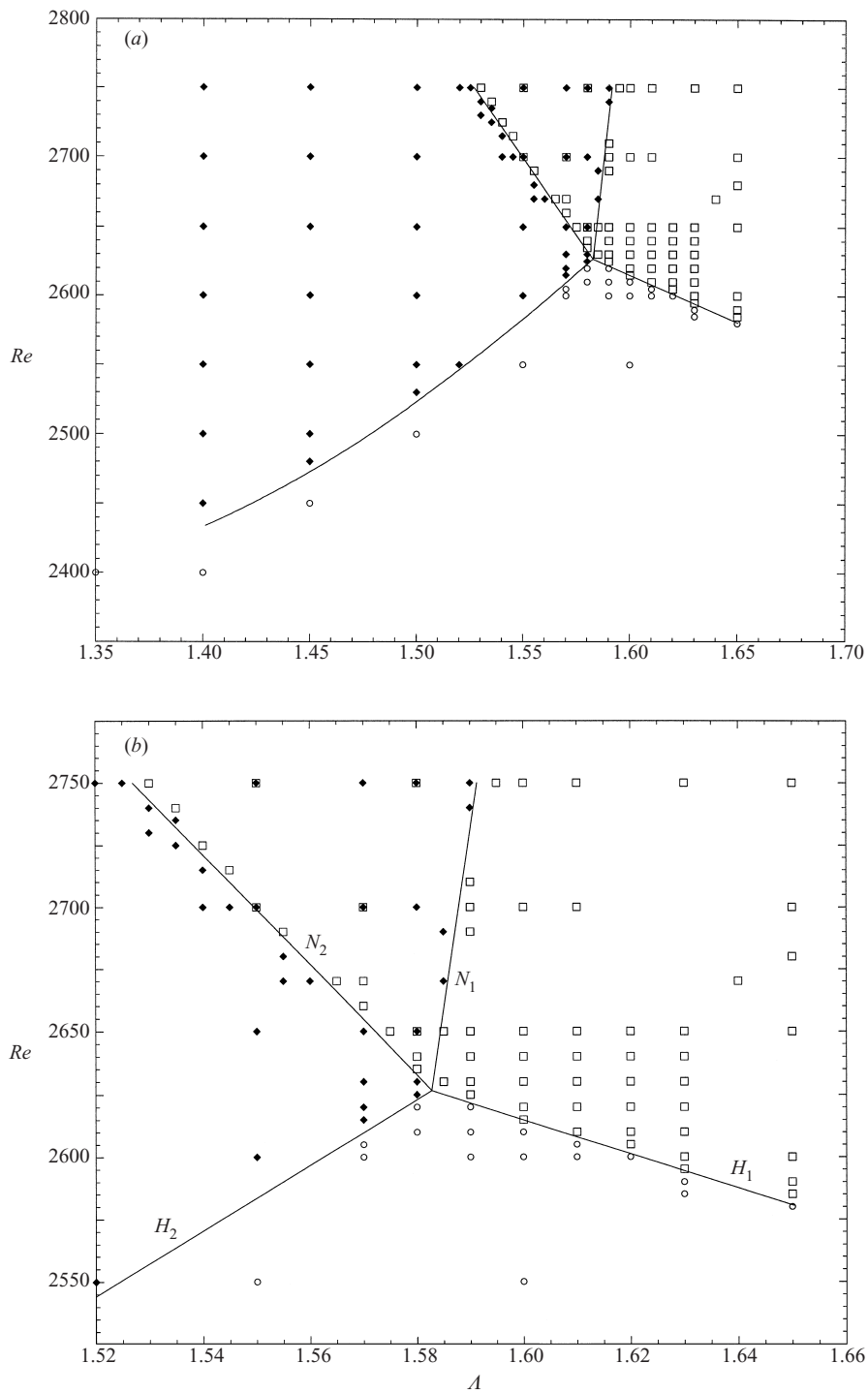


FIGURE 2. (a) Loci of solution types in  $(A, Re)$ -space;  $\blacklozenge$ ,  $m = 2$  rotating waves;  $\square$ ,  $m = 0$  limit cycles;  $\circ$ ,  $m = 0$  steady states. (b) Close-up of (a) including estimates of the Hopf curves for  $m = 0$  limit cycles ( $H_1$ ) and  $m = 2$  rotating waves ( $H_2$ ), and the Naimark-Sacker curves where the rotating wave loses stability ( $N_1$ ) and the limit cycle loses stability ( $N_2$ ).

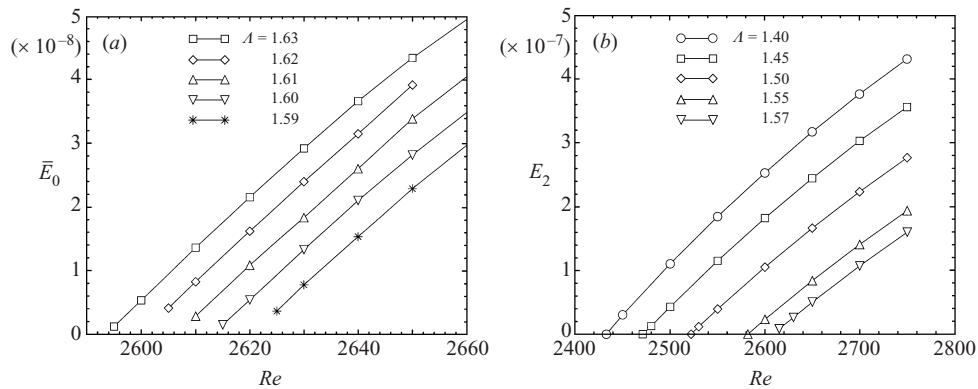


FIGURE 3. (a)  $\mathcal{L}_2$ -norm squared of the amplitude of the oscillations of the axisymmetric periodic solutions (denoted  $E_0$ ), and (b)  $\mathcal{L}_2$ -norm squared of the  $m = 2$  mode corresponding to the rotating wave (denoted  $E_2$ ), for different  $A$  values.

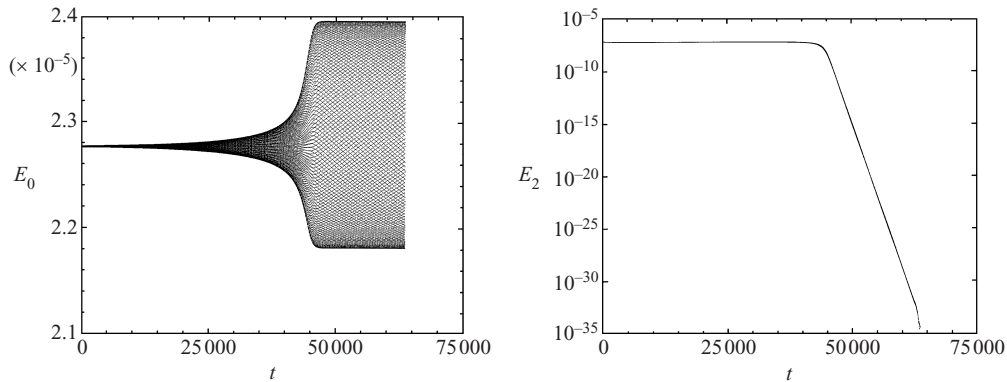


FIGURE 4. Time evolution of the kinetic energies  $E_0$  and  $E_2$  for  $Re = 2690$  and  $A = 1.590$ , starting from the  $m = 2$  solution at  $Re = 2690$ ,  $A = 1.585$ .

by decreasing  $A$  until it becomes unstable and evolves to the  $m = 2$  rotating wave; figure 5 shows this evolution for  $Re = 2700$ ,  $A = 1.54$ , starting with the stable  $m = 0$  solution at  $Re = 2700$ ,  $A = 1.55$  as the initial condition. The precision to which these are detected can be increased by bisection. They cannot be detected by looking at the amplitudes of the axisymmetric limit cycle or rotating wave solution, because as we have shown in figure 1, both have finite amplitude and frequency. It is the unstable two-torus that emerges at these bifurcations, with zero amplitude, growing as the square root of the distance from these curves in parameter space. The coexistence region bound by  $N_1$  and  $N_2$  is a wide wedge in parameter space.

One implication of the double-Hopf region bound by the Naimark–Sacker curves is that when one performs a parameter sweep (either numerically or experimentally) in the neighbourhood of the double Hopf, the multiplicity of solutions means that the observed state could be either of the two, depending on initial conditions and other perturbations. Linear stability analysis of the basic state alone does not help here; it can locate the double Hopf but tells you nothing of where the Naimark–Sacker curves lie (nor which of the many possible double Hopf scenarios is appropriate). This situation is further compounded for the experimental sweeps as the growth rates near the Naimark–Sacker curves are extremely small (zero on the curves), and so

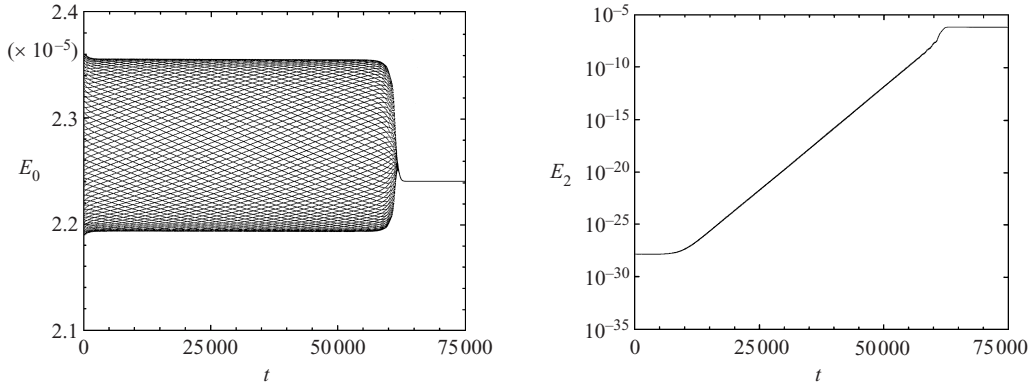


FIGURE 5. Time evolution of the kinetic energies  $E_0$  and  $E_2$  for  $Re = 2700$  and  $A = 1.54$ , starting from the  $m = 0$  solution at  $Re = 2700$ ,  $A = 1.55$ .

transient unstable states may appear to be stable for extensive periods of time (see figures 4 and 5).

The limit cycle period is  $20 \pm 5\%$  over the range of parameters shown in figure 2. The variation in the precession period of the  $m = 2$  rotating wave is much larger: at around  $A = 1.55$  the sense of precession changes from prograde to retrograde with respect to the rotating disk. Generically, in systems with  $SO(2)$  symmetry, standing waves are not expected, but in the two-dimensional parameter space  $(Re, A)$  they can exist along a (one-dimensional) curve, where the precession changes sense. The period goes to infinity as this curve is approached. The presence of a standing wave in the neighbourhood of our double Hopf point is coincidental.

#### 4.2. Physical description of the flow states

The basic state in this problem, steady and axisymmetric for low  $Re$ , is non-trivial, having detailed structure in both  $r$  and  $z$ , and must be computed numerically. The main features of this flow consist of a thin Ekman-type boundary layer on the rotating endwall at  $z = 0$ , whose thickness scales with  $Re^{-1/2}$ ; the presence of the stationary sidewall turns the Ekman layer into the interior producing a swirling axisymmetric jet. These features can be seen in figure 6, where the contours of the three velocity components of a basic state at  $Re = 2605$  and  $A = 1.57$  are presented. This jet advects angular momentum fluid into the interior and the top stationary endwall turns this fluid in towards  $r = 0$ , leading to a centrifugally unstable situation. The fluid near the axis returns slowly to the Ekman layer on the bottom rotating disk, and undergoes undulations due to centrifugal effects. These undulations, at larger aspect ratios, lead to the formation of recirculation bubbles (Escudier 1984; Brown & Lopez 1990).

When the aspect ratio is larger than  $A_{dH} = 1.5828$ , the basic state loses stability to an axisymmetric limit cycle. However due to the dynamics associated with the double Hopf bifurcation described above, the axisymmetric limit-cycle state can be found to be stable at lower aspect ratios. This follows from the fact that the Naimark–Sacker curves,  $N_1$  and  $N_2$ , have positive and negative slopes, respectively (see figure 2). Such a case is illustrated in figure 7, consisting of contours of the three components of velocity at six phases over a complete temporal period ( $T = 19.1$ ). The oscillation consists of a pulsation of the flow with maximum amplitude in the vicinity of the near-axis undulation described above for the basic state. This oscillatory mode is of

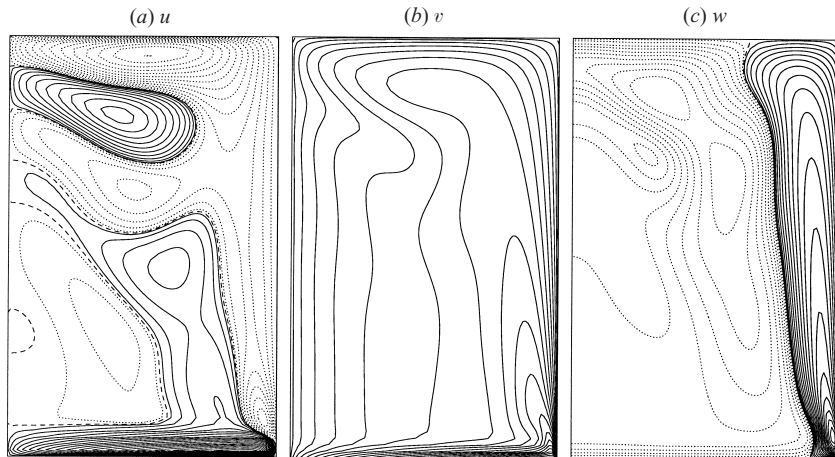


FIGURE 6. Contours of  $u$ ,  $v$ , and  $w$  for the axisymmetric steady-state solution at  $Re = 2605$ ,  $A = 1.57$ ; for  $u$  and  $w$ , solid (dotted) contours are positive (negative) with values  $\pm 0.15(i/20)^2$  for  $i \in [1, 20]$ , and the zero contour is dashed, and for  $v$  the contours are  $(i/20)^2$ . The contour plots in this figure, as well as in figures 7, 8 and 11, are in the meridional plane  $\{(r, \theta, z) : r \in [0, 1], \theta = 0, z \in [0, A]\}$ , so the left boundary is the axis, the right boundary is the stationary cylinder wall, the top is stationary, and the bottom is the rotating endwall.

the same branch of solutions as others have described for larger aspect ratios (e.g. Lopez & Perry 1992; Sorensen & Christensen 1995; Lopez *et al.* 2001a).

In figure 8 the  $m = 2$  rotating wave solution that coexists with the  $m = 0$  solution just described is shown. It consists of contours of the three components of velocity at six phases over an azimuthal period ( $\pi$  radians). As this solution is a rotating wave, its three-dimensional structure is time independent, and rotates as a fixed structure with the precession frequency. Note that the components  $v$  and  $w$  show very little variation with  $\theta$  in contrast with the  $m = 0$  state, where all three components have comparable variations.

Near the bifurcation, the difference between the stable bifurcated state and the unstable basic state is proportional to the bifurcating eigenmode. Since near the bifurcation the energy of this eigenmode is vanishingly small and that of its harmonics is even smaller (see table 1), we obtain a very good approximation to the eigenmode by setting to zero the  $m = 0$  component of the bifurcated state. We denote by  $u_p$ ,  $v_p$  and  $w_p$  the radial, azimuthal and axial components of the ‘perturbation’ velocity field, obtained by setting to zero the  $m = 0$  mode in the Fourier expansion of the nonlinear velocity field. Figure 9 shows contours of  $u_p$ ,  $v_p$  and  $w_p$  in  $(r, \theta)$ -planes at four equispaced  $z$ -levels for the  $m = 2$  rotating wave solution at ( $Re = 2630$ ,  $A = 1.58$ ), a point in parameter space very close to the double Hopf point ( $Re = 2626.6$ ,  $A = 1.5828$ ). We have compared the corresponding contour plots at a point further away from the double Hopf point ( $Re = 2750$ ,  $A = 1.58$ ) and the only discernible difference is that the magnitude of the perturbation is larger by about a factor of five for the larger  $Re$  case, but the detailed spatial structure remains essentially unchanged. We have found this to be true over a wide range of parameter space (the range shown in figure 2). The spatial structure of the perturbation is quite complex in  $(r, z)$ . The contours suggest that they are composed of three sets of four spiral arms; the four being the pairs (due to the  $m = 2$  wavenumber) of positive and negative perturbations. One set is localized deep in the sidewall boundary layer, a second set

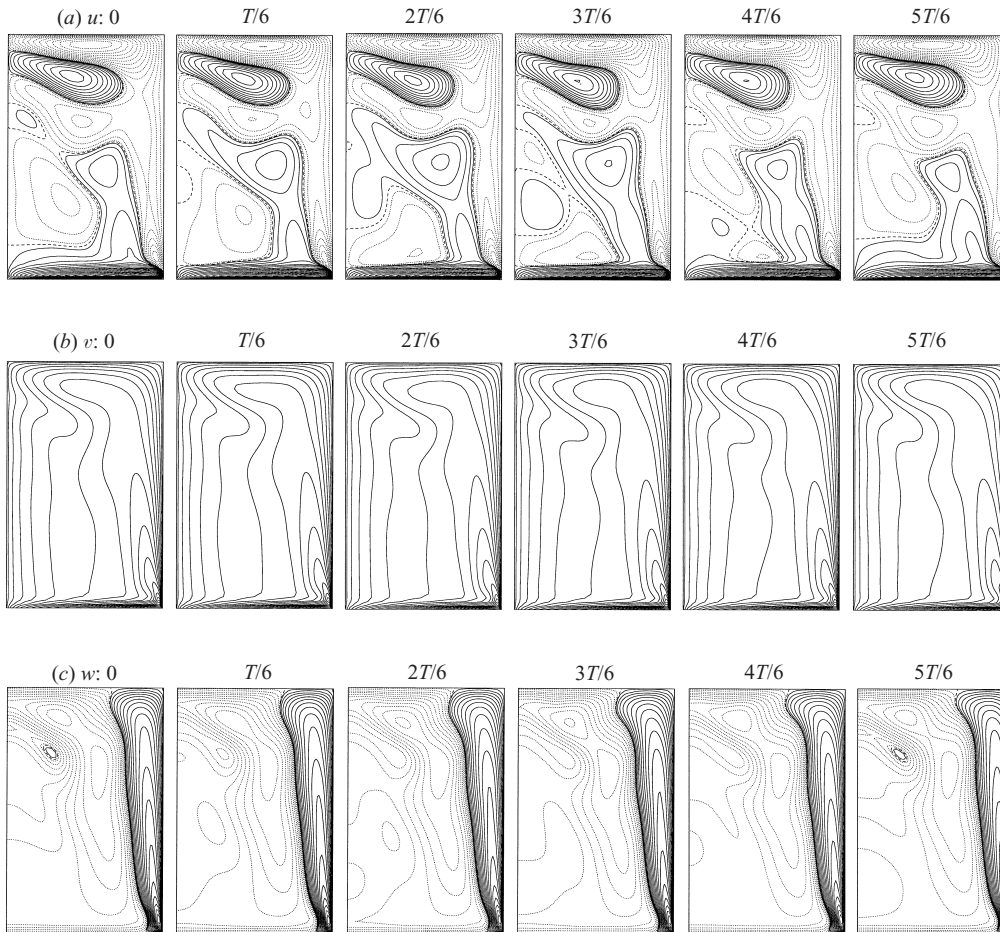


FIGURE 7. Contours of  $u$ ,  $v$ , and  $w$  at phases over one period, as indicated, for the axisymmetric limit-cycle solution at  $Re = 2700$ ,  $A = 1.57$ ; for  $u$  and  $w$ , solid (dotted) contours are positive (negative) with values  $\pm 0.15(i/20)^2$  for  $i \in [1, 20]$ , and the zero contour is dashed, and for  $v$  the contours are  $(i/20)^2$ .

is localized about the maximum of the  $v$  velocity of the basic state, and the third is localized about the axis. The three sets of spiral arms have differing pitch angles, which vary with  $z$ , and the pitch of the set about the axis is in the opposite sense compared to the other two.

In figure 10, isosurfaces of the velocity perturbations of the  $m = 2$  rotating wave solution at ( $Re = 2750$ ,  $A = 1.58$ ) in three dimensions are presented to help visualize the complicated spatial structure associated with the spiral arms. In parts (a)–(c) of the figure, the isolevel is set to just above zero (the zero level isosurface contains too much numerical noise) and it separates the regions of three-space into those with positive and negative perturbations. The figures give a reasonable indication of how the spiral arms are interconnected. Parts (d)–(f) of figure 10 have isolevels set at about 60% of the maximum perturbation, and clearly indicate where the maximum perturbations are located. They are located near the top stationary endwall and away from the axis, essentially where the swirling jet, resulting from the turning of the Ekman layer into the interior, is turned in towards the axis by the presence of the top

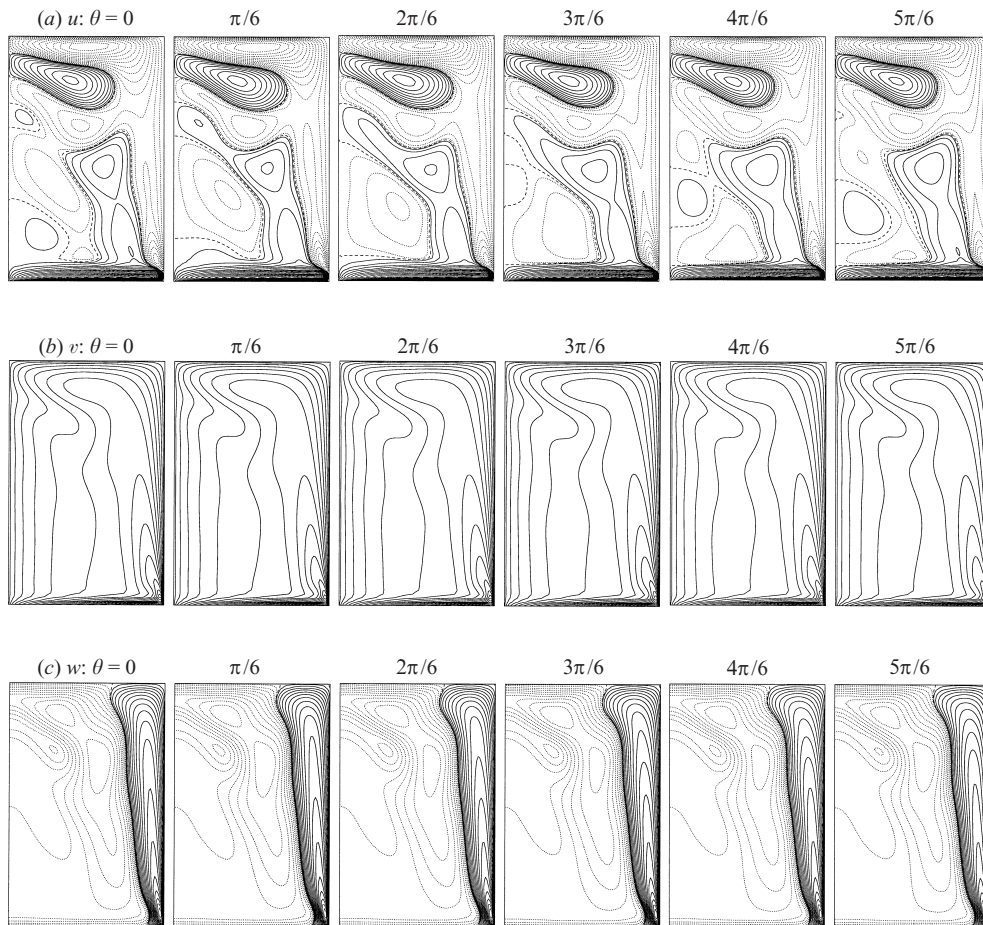


FIGURE 8. Contours of  $u$ ,  $v$ , and  $w$  at different angles  $\theta$ , as indicated, for the rotating wave solution at  $Re = 2700$ ,  $A = 1.57$ ; for  $u$  and  $w$ , solid (dotted) contours are positive (negative) with values  $\pm 0.15(i/20)^2$  for  $i \in [1, 20]$ , and the zero contour is dashed, and for  $v$  the contours are  $(i/20)^2$ .

endwall. The destabilization of the basic axisymmetric steady state, in this region of parameter space, is associated with instabilities of the swirling jet. This is the case for both the bifurcation to the  $m = 0$  limit cycle and to the  $m = 2$  rotating wave states, as is shown in the next paragraph. The central vortex core does not seem to play a role.

In the region bounded by the two Naimark–Sacker curves,  $N_1$  and  $N_2$  in figure 2, both the  $m = 0$  limit cycle and the  $m = 2$  rotating wave solutions coexist and are stable. In order to better understand how the steady basic state loses stability to each of these states, we now look at the kinetic energies of its respective perturbations. The time-average of a periodic quantity  $f$  is

$$\langle f \rangle = \frac{1}{T} \int_0^T f dt,$$

where  $T$  is the period. The time-averages,  $\langle \mathbf{u} \rangle$ , of either bifurcated state will be very close to the underlying basic state, since we are looking at nonlinear solutions close to the bifurcation point. Then the perturbation field is  $\mathbf{u} - \langle \mathbf{u} \rangle$ , and its average kinetic

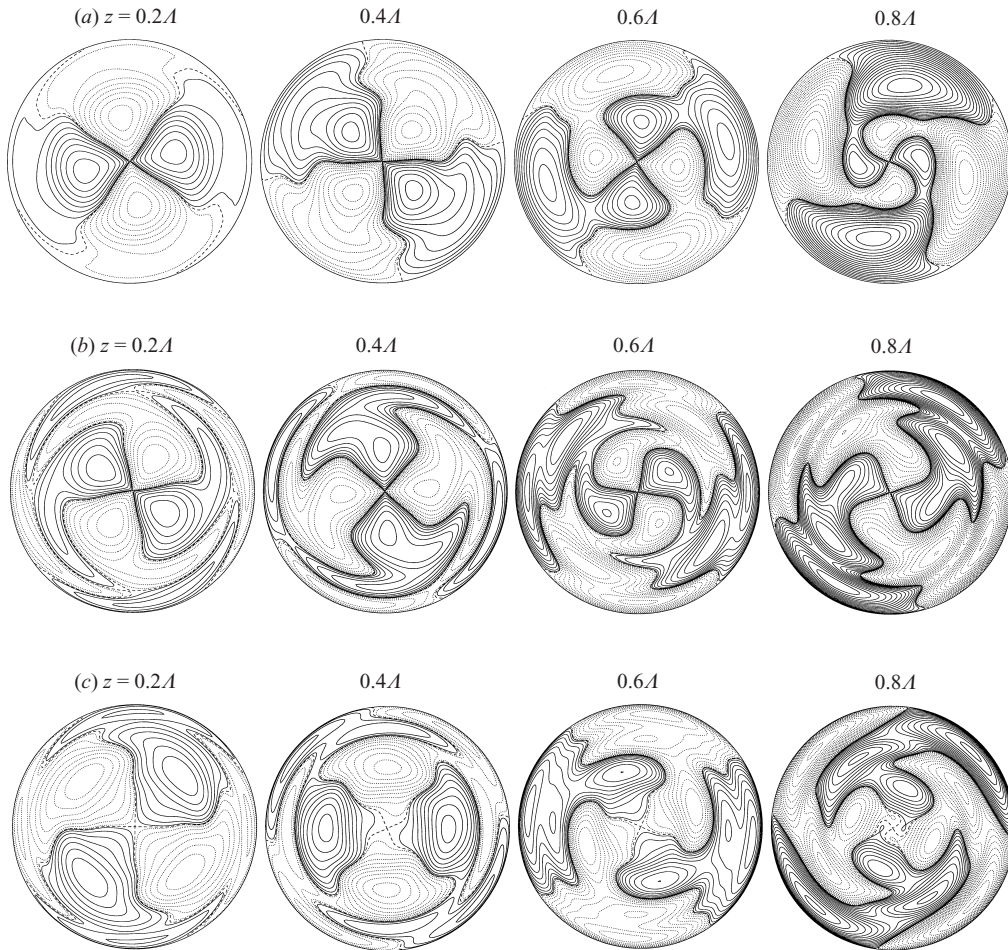


FIGURE 9. Contours of (a)  $u_p$ , (b)  $v_p$ , and (c)  $w_p$ , at different heights  $z$ , as indicated, for the rotating wave solution at  $Re = 2630$ ,  $A = 1.58$ ; solid (dotted) contours are positive (negative) with values  $\pm 0.002(i/20)^2$  for  $i \in [1, 20]$ , and the zero contour is dashed.

energy is  $\langle 0.5|\mathbf{u} - \langle \mathbf{u} \rangle|^2 \rangle$ . In figure 11, the time averages and average kinetic energies of the perturbation fields for coexisting  $m = 0$  limit cycle and  $m = 2$  rotating wave at ( $Re = 2700$ ,  $A = 1.57$ ) are presented. Note that for a rotating wave solution, a time average at a fixed azimuthal angle is equivalent to an average over the angle at a fixed time. Further, in the neighbourhood of the Hopf bifurcation from which it emerges, the time average is equivalent to setting its  $m = 0$  Fourier mode to zero. As expected, due to being close to the respective Hopf curves, the averages of the two states agree to a large extent (see parts (a) and (c) of figure 11), indicating that these averages are a good approximation to the underlying unstable basic state. The kinetic energies of the perturbations to each respective state however differ in two fundamental respects. First, they differ in maximum kinetic energy by a factor of about 2.6, the energy of the  $m = 0$  perturbation being the larger. Second, the maxima in average kinetic energy occur in different locations. For the axisymmetric limit cycle (see figure 11a, b), the swirling jet seems to turn at the stationary top and the maximum in the perturbation kinetic energy is associated with the jet colliding with itself as it approaches the axis and is turned back into the interior. This results in an axisymmetric pulsation

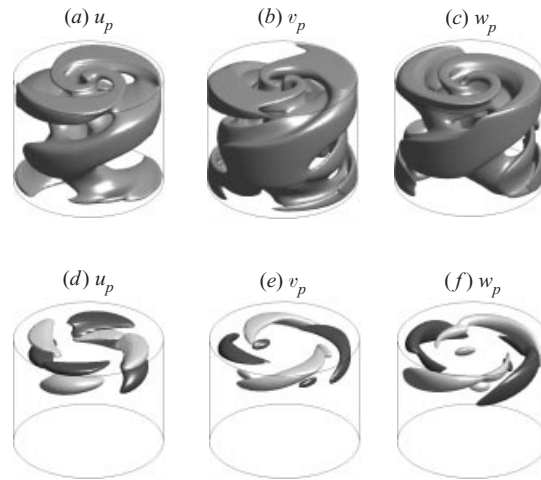


FIGURE 10. Isosurfaces of the velocity perturbations of the  $m = 2$  rotating wave solution at  $Re = 2750$ ,  $A = 1.58$ : for (a), (b) and (c) the level is zero plus 1% of maximum, and for (d), (e) and (f) the level is at 60% of maximum.

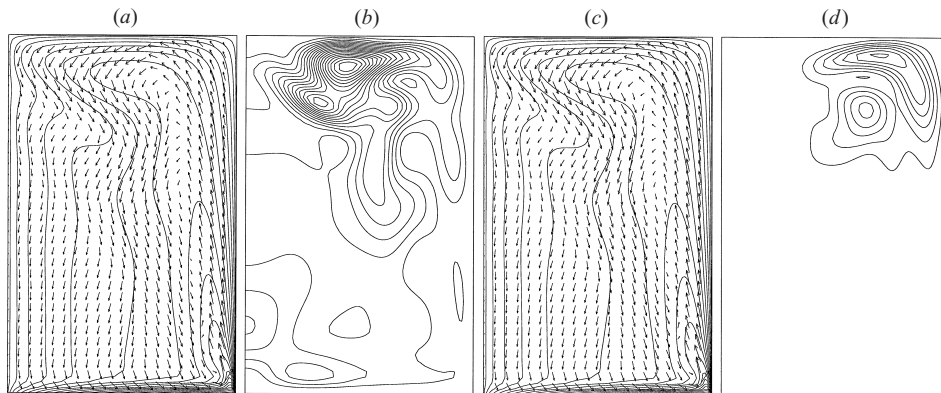


FIGURE 11. (a) Contours of the azimuthal component of  $\langle \mathbf{u} \rangle$  together with arrows representing its radial and axial components, for the  $m = 0$  limit cycle; (b) contours of the kinetic energy of the perturbation field,  $\langle 0.5|\mathbf{u} - \langle \mathbf{u} \rangle|^2 \rangle$ , for the solution in (a); (c) and (d) same as (a) and (b), but for the  $m = 2$  rotating wave; both cases are at  $Re = 2700$  and  $A = 1.57$ . The contour levels in (a) and (c) are set as  $(i/20)^2$ ,  $i \in [0, 20]$ , the arrow lengths are scaled by  $(|\mathbf{u}|/\max|\mathbf{u}|)^{0.4}$ , and in (b) and (d) the contour levels are set as  $5 \times 10^{-5}(i/20)$ ,  $i \in [0, 20]$ .

localized about the axis, and is associated with the periodic appearance of a small toroidal recirculation zone, as seen in figure 7(c). With the rotating wave however (see figure 11c,d), this maximum is associated with the collision of the swirling jet with the stationary top causing the flow to turn into towards the axis. This is seen to break the  $SO(2)$  symmetry, resulting in the  $m = 2$  rotating wave, clearly depicted in figure 10.

## 5. Conclusions

For the two-parameter system of a flow in a cylinder driven by the rotation of an endwall, we have located a codimension-2 bifurcation corresponding to a double Hopf bifurcation. This codimension-2 bifurcation is very rich, allowing for several different

scenarios depending on the particulars of the system at hand. By a comprehensive two-parameter exploration about this point, and our normal form analysis showing that resonances are not possible in this  $SO(2)$  equivariant system, we have identified precisely to which scenario this case corresponds. This is one of a very small number of fluid systems where the dynamics associated with the double Hopf bifurcation has been fully explored. This has only been possible by using a very efficient and accurate three-dimensional Navier–Stokes solver.

The signature of a double Hopf bifurcation is mode interactions, and the presence of multiple modes is due to competition between distinct instability mechanisms. By exploring in detail the three-dimensional structure of the flow, and the average kinetic energies of the perturbations, we have identified the two mechanisms that compete in the neighbourhood of the double Hopf bifurcation. Both are associated with the jet that is formed when the Ekman layer on the rotating endwall is turned by the stationary sidewall. For the rotating wave state, the mechanism is associated with collision of the jet with the top stationary endwall leading to instability (an  $m = 2$  rotating wave), whereas for the axisymmetric limit-cycle state, the jet turns at the top without causing instability, but as it collides with itself near the axis, an instability leading to an axisymmetric pulsation results. For parameter values below the two Hopf curves, the jet in the basic steady state is able to negotiate all these turns without any instability.

Another characteristic feature of the double Hopf bifurcation is the existence of two-tori states (in our problem these correspond to unstable modulated rotating waves). This two-torus is born at the double Hopf point and exists in a wide region of parameter space, delineated by the two Naimark–Sacker curves. Although this two-torus is unstable, it plays a fundamental role in the dynamics; the two bifurcated stable solutions, the  $m = 0$  limit cycle and the  $m = 2$  rotating wave, lose stability by colliding with the two-torus at their respective Naimark–Sacker curves. Inside this region, the multiplicity of states can make interpretations of experiments and numerical simulations difficult, particularly as the time scales associated with the growth rates can be very large. A short time experiment may identify as stable a state that is in fact unstable; this is typical behaviour as the Naimark–Sacker curves are crossed.

This work was partially supported by DGICYT grant PB97-0685 and Generalitat de Catalunya grant 1999BEAI400103 (Spain), and NSF grants INT-9732637, CTS-9908599 and DMS-0074283 (USA).

### Appendix. Normal form of the double Hopf bifurcation with $SO(2)$ symmetry

The technique of Iooss & Adelmeyer (1998), which provides a clear and simple method to obtain normal forms, incorporating symmetry considerations, is now used for the double Hopf bifurcation with the  $SO(2)$  symmetry group. In the codimension-one Hopf bifurcation, the presence of  $SO(2)$  symmetry does not alter the generic normal form, and the same is true for the double Hopf without resonance. However it is important to specify what the resonance conditions are, because as we shall see,  $SO(2)$  inhibits resonance. Resonance is only possible if both the temporal modes (imaginary parts of the eigenvalues  $\omega_{1,2}$ ) and the spatial modes (azimuthal wavenumbers  $m_{1,2}$ ) satisfy the resonance condition  $\omega_2/\omega_1 = m_2/m_1 = p/q$ , where  $p$  and  $q$  are positive irreducible integers.

Let us assume that we have a steady, axisymmetric basic flow that undergoes a double Hopf bifurcation and the corresponding eigenvectors, in cylindrical polar coordinates  $(r, \theta, z)$ , are of the form

$$\mathbf{v}_1 = \mathbf{u}_1(r, z)e^{i(m_1\theta + \omega_1 t)}, \quad \mathbf{v}_2 = \mathbf{u}_2(r, z)e^{i(m_2\theta + \omega_2 t)}, \quad (\text{A } 1)$$

plus the corresponding complex conjugates, where  $\omega_{1,2} > 0$ , and  $m_{1,2} \in \mathbb{Z}$  (positive, negative or zero integers). The centre manifold theorem states that in a neighbourhood of the bifurcation point, the velocity field can be written as

$$\mathbf{v} = \eta_1(t)\mathbf{v}_1 + \eta_2(t)\mathbf{v}_2 + \bar{\eta}_1(t)\bar{\mathbf{v}}_1 + \bar{\eta}_2(t)\bar{\mathbf{v}}_2 + \text{h.o.t.}, \quad (\text{A } 2)$$

where  $\eta_{1,2} \in \mathbb{C}$  are complex amplitudes, overbars indicate complex conjugation, and h.o.t. refers to higher-order terms, at least second order in the amplitudes. The centre manifold is four-dimensional and  $\eta_{1,2}, \bar{\eta}_{1,2}$  are its coordinates. The action of  $SO(2)$  on these coordinates is

$$R_\alpha(\eta_1, \eta_2, \bar{\eta}_1, \bar{\eta}_2) = (e^{im_1\alpha}\eta_1, e^{im_2\alpha}\eta_2, e^{-im_1\alpha}\bar{\eta}_1, e^{-im_2\alpha}\bar{\eta}_2), \quad (\text{A } 3)$$

where  $R_\alpha$  is an azimuthal rotation of angle  $\alpha (R_\alpha : \theta \rightarrow \theta + \alpha)$ .

The normal form theorem says that by a suitable analytic change of coordinates preserving the symmetry ( $\eta \rightarrow z + \text{h.o.t.}$ ), the dynamical system in a neighbourhood of the fixed point (steady, axisymmetric base state) in the centre manifold can be cast in the form

$$\dot{z}_i = i\omega_i z_i + P_i(z_1, z_2, \bar{z}_1, \bar{z}_2, \mu), \quad (\text{A } 4)$$

plus complex conjugate, for  $i = 1, 2$ . The functions  $P_i$  are second order in  $z$  for  $\mu = 0$  and satisfy

$$P(e^{tL_o^*} z) = e^{tL_o^*} P(z), \quad P(R_\alpha z) = R_\alpha P(z), \quad \forall t, \alpha \in \mathbb{R}, \quad (\text{A } 5a, b)$$

where  $L_o$  is the linear part of the dynamical system at criticality and  $L_o^*$  is the corresponding adjoint operator. We have used vector notation  $z = (z_1, z_2, \bar{z}_1, \bar{z}_2)$ ,  $P = (P_1, P_2, \bar{P}_1, \bar{P}_2)$  in order to keep the expressions compact. In this notation the matrices  $e^{tL_o^*}$  and  $R_\alpha$  are diagonal:

$$e^{tL_o^*} = \text{diag}(e^{-i\omega_1 t}, e^{-i\omega_2 t}, e^{i\omega_1 t}, e^{i\omega_2 t}), \quad (\text{A } 6)$$

$$R_\alpha = \text{diag}(e^{im_1\alpha}, e^{im_2\alpha}, e^{-im_1\alpha}, e^{-im_2\alpha}). \quad (\text{A } 7)$$

Equation (A 5a) gives the simplest form of  $P$  attainable using the structure of the linear part  $L_o$ , and (A 5b) gives the additional constraints on  $P$  imposed by the symmetry group  $SO(2)$ . As the actions of  $e^{tL_o^*}$  and  $R_\alpha$  are identical (replacing  $-\omega_i t$  with  $m_i \alpha$ ), the symmetry group  $SO(2)$  does not alter the normal form, except in the case of resonance.

Let  $z_1^k z_2^l \bar{z}_1^r \bar{z}_2^s$  be an admissible monomial in  $P_1$ ; it must satisfy equations (A 5), i.e.

$$(k - r - 1)\omega_1 + (l - s)\omega_2 = 0, \quad (\text{A } 8a)$$

$$(k - r - 1)m_1 + (l - s)m_2 = 0. \quad (\text{A } 8b)$$

If  $\omega_2/\omega_1 \notin \mathbb{Q}$ , the only solution of the first equation (and of the system) is  $k = r + 1$ ,  $l = s$ , which coincides with the generic non-symmetric case analysed in Kuznetsov (1998). The normal form is then

$$P_1 = z_1 Q_1, \quad P_2 = z_2 Q_2, \quad (\text{A } 9)$$

where  $Q_i(|z_1|^2, |z_2|^2)$ . This case corresponds to the normal form (2.1), with  $z_1 = r_1 e^{i\phi_1}$

and  $z_2 = r_2 e^{i\phi_2}$ . In (2.1), some of the fifth-order terms have been simplified using the non-degeneracy condition  $p_{ij} \neq 0$  (Kuznetsov 1998).

If  $\omega_2/\omega_1 = p/q \in \mathbb{Q}$ , we are in the temporal resonant case, and additional monomials may appear in the normal form due to the first equation in (A 8):

$$P_1 = z_1 Q_{11} + \bar{z}_1^{p-1} z_2^q Q_{12}, \quad P_2 = z_2 Q_{21} + z_1^p \bar{z}_2^{q-1} Q_{22}, \quad (\text{A } 10)$$

where the  $Q_{ij}$  are functions of  $|z_1|^2$ ,  $|z_2|^2$ ,  $z_1^p \bar{z}_2^q$ , and  $\bar{z}_1^p z_2^q$ ; this is in accordance with Theorem 4.2 on p. 445 in Golubitsky, Stewart & Schaeffer (1988). Now we determine whether these are consistent with (A 8b). If  $m_1 = m_2 = 0$ , (A 8b) is identically zero, the centre manifold lies in an  $SO(2)$ -equivariant subspace, and the symmetry does not play any role (in a neighbourhood of the bifurcation). This is the generic (non-symmetric) resonant case and (A 10) is its normal form. If one of the  $m_i$  is zero and the other is not, (A 8b) implies  $k = r + 1$  and  $l = s$ , the resonant terms are suppressed by the presence of the symmetry and the normal form is (A 9). If both  $m_i$  are non-zero, the system (A 8) has additional solutions (resonant terms) if and only if  $m_2 \omega_1 - m_1 \omega_2 = 0$ . Again, the presence of  $SO(2)$  inhibits resonance and the normal form is (A 9), except when the spatial and temporal modes satisfy the same resonance condition  $\omega_2/\omega_1 = m_2/m_1 = p/q$ , and then the normal form is (A 10).

#### REFERENCES

- BLACKBURN, H. M. & LOPEZ, J. M. 2000 Symmetry breaking of the flow in a cylinder driven by a rotating endwall. *Phys. Fluids* **12**, 2698–2701.
- BROWN, G. L. & LOPEZ, J. M. 1990 Axisymmetric vortex breakdown: Part 2. Physical mechanisms. *J. Fluid Mech.* **221**, 553–576.
- CHORIN, A. J. 1968 Numerical solution of the Navier–Stokes equations. *Math. Comp.* **22**, 745–762.
- DAUBE, O. & SØRENSEN, J. N. 1989 Simulation numérique de l'écoulement périodique axisymétrique dans une cavité cylindrique. *C. R. Acad. Sci. Paris* **308**, 463–469.
- ESCUDIER, M. P. 1984 Observations of the flow produced in a cylindrical container by a rotating endwall. *Exps. Fluids* **2**, 189–196.
- GELFGAT, A. Y., BAR-YOSEPH, P. Z. & SOLAN, A. 1996 Stability of confined swirling flow with and without vortex breakdown. *J. Fluid Mech.* **311**, 1–36.
- GELFGAT, A. Y., BAR-YOSEPH, P. Z. & SOLAN, A. 2001 Three-dimensional instability of axisymmetric flow in a rotating lid-cylinder enclosure. *J. Fluid Mech.* **438**, 363–377.
- GOLUBITSKY, M., STEWART, I. & SCHAEFFER, D. G. 1988 *Singularities and Groups in Bifurcation Theory*, Vol. II. Springer.
- GUCKENHEIMER, J. & HOLMES, P. 1986 *Nonlinear Oscillations, Dynamical Systems, and Bifurcations of Vector Fields*. Springer.
- IOOSS, G. & ADELMAYER, M. 1998 *Topics in Bifurcation Theory and Applications*, 2nd edn. World Scientific.
- KNOBLOCH, E. 1994 Bifurcations in rotating systems. In *Lectures on Solar and Planetary Dynamos* (ed. M. R. E. Proctor & A. D. Gilbert), pp. 331–372. Cambridge University Press.
- KNOBLOCH, E. 1996 Symmetry and instability in rotating hydrodynamic and magnetohydrodynamic flows. *Phys. Fluids* **8**, 1446–1454.
- KNOBLOCH, E. & PROCTOR, M. R. E. 1988 The double Hopf bifurcation with 2:1 resonance. *Proc. R. Soc. Lond. A* **415**, 61–90.
- KUZNETSOV, Y. A. 1998 *Elements of Applied Bifurcation Theory*, 2nd edn. Springer.
- LOPEZ, J. M. 1990 Axisymmetric vortex breakdown: Part 1. Confined swirling flow. *J. Fluid Mech.* **221**, 533–552.
- LOPEZ, J. M., MARQUES, F. & SANCHEZ, J. 2001a Oscillatory modes in an enclosed swirling flow. *J. Fluid Mech.* **439**, 109–129.
- LOPEZ, J. M., MARQUES, F. & SHEN, J. 2001b An efficient spectral-projection method for the Navier–Stokes equations in cylindrical geometries II. Three dimensional cases. *J. Comput. Phys.* Accepted for publication.

- LOPEZ, J. M. & PERRY, A. D. 1992 Axisymmetric vortex breakdown: Part 3. Onset of periodic flow and chaotic advection. *J. Fluid Mech.* **234**, 449–471.
- LOPEZ, J. M. & SHEN, J. 1998 An efficient spectral-projection method for the Navier–Stokes equations in cylindrical geometries I. Axisymmetric cases. *J. Comput. Phys.* **139**, 308–326.
- LUGT, H. J. & ABBOUD, M. 1987 Axisymmetric vortex breakdown with and without temperature effects in a container with a rotating lid. *J. Fluid Mech.* **179**, 179–200.
- NEITZEL, G. P. 1988 Streak-line motion during steady and unsteady axisymmetric vortex breakdown. *Phys. Fluids* **31**, 958–960.
- ORSZAG, S. A. & PATERA, A. T. 1983 Secondary instability of wall-bounded shear flows. *J. Fluid Mech.* **128**, 347–385.
- RENARDY, M., RENARDY, Y., SURESHKUMAR, R. & BERIS, A. N. 1996 Hopf–Hopf and steady–Hopf mode interactions in Taylor–Couette flow of an upper convected Maxwell liquid. *J. Non-Newtonian Fluid Mech.* **63**, 1–31.
- SHEN, J. 1994 Efficient spectral-Galerkin method I. Direct solvers for second- and fourth-order equations by using Legendre polynomials. *SIAM J. Sci. Comput.* **15**, 1489–1505.
- SHEN, J. 1997 Efficient spectral-Galerkin methods III. Polar and cylindrical geometries. *SIAM J. Sci. Comput.* **18**, 1583–1604.
- SORENSEN, J. N. & CHRISTENSEN, E. A. 1995 Direct numerical simulation of rotating fluid flow in a closed cylinder. *Phys. Fluids* **7**, 764–778.
- SOTIROPOULOS, F. & VENTIKOS, Y. 2001 The three-dimensional structure of confined swirling flows with vortex breakdown. *J. Fluid Mech.* **426**, 155–175.
- SPOHN, A., MORY, M. & HOPFINGER, E. J. 1998 Experiments on vortex breakdown in a confined flow generated by a rotating disk. *J. Fluid Mech.* **370**, 73–99.
- STEVENS, J. L., LOPEZ, J. M. & CANTWELL, B. J. 1999 Oscillatory flow states in an enclosed cylinder with a rotating endwall. *J. Fluid Mech.* **389**, 101–118.
- TEMAM, R. 1969 Sur l’approximation de la solution des équations de Navier–Stokes par la méthode des pas fractionnaires II. *Arch. Rat. Mech. Anal.* **33**, 377–385.